Published in final edited form as:
Opt Express. 2007 October 1; 15(20): 13375–13387.

Full range complex spectral domain optical coherence tomography without additional phase shifters

Bernhard Baumann, **Michael Pircher**, **Erich Götzinger**, and **Christoph K. Hitzenberger**
Center for Biomed. Eng. and Physics, Medical University of Vienna, Währinger Str. 13, A-1090 Vienna, Austria, bernhard.baumann@meduniwien.ac.at, christoph.hitzenberger@meduniwien.ac.at

Abstract

We demonstrate a new full range complex spectral domain optical coherence tomography (FRC SD-OCT) method. Other than FRC SD-OCT systems reported in literature, which employed devices such as electro-/acousto optic modulators or piezo-driven mirrors providing the phase modulations necessary for retrieval of the complex-valued signal, the system presented works without any additional phase shifting device. The required phase shift is introduced by the galvanometer scanner used for transversally scanning the sample beam. By means of a slight displacement of the probe beam with respect to the scanning mirror's pivot axis, the sample arm length and thus the phase is continuously modulated as the beam is scanned in lateral direction. From such modulated spectral data, the complex-valued data yielding a twofold increase of accessible depth range can be calculated using an algorithm based on the Hilbert transform. To demonstrate the performance of our method quantitative measurements of the suppression of mirror images as a function of induced phase shift were performed. In order to validate the FRC SD-OCT technique for high-speed imaging of biological tissue, we present full-range images of the human anterior chamber in vivo.

1. Introduction

Optical coherence tomography (OCT) has developed to a powerful technique to image biological samples [1,2]. In recent years, the focus of new developments has shifted towards spectral domain (SD) OCT and swept-source (SS) OCT since it has been shown that these versions of OCT have huge advantages in terms of acquisition speed and sensitivity, as compared to time domain optical coherence tomography (TD-OCT) [3,4,5].

In SD-OCT depth resolved information is encoded in the cross spectral density function measured with a spectrometer located in the detection arm of an interferometer [6,7]. A drawback of this method is that since the detected spectral density is a real function and therefore its Fourier transform is Hermitian, the reconstructed image is symmetrical about zero path difference. As a consequence one cannot distinguish between negative and positive optical path differences with respect to the reference mirror. These effects are of minor importance for measuring thin objects (e. g. retina), because the reference arm can be shifted to a position where the mirror images do not affect the image of the measured object. However, if one wants to measure objects with larger depth extension where the whole measurement range is needed (e. g. anterior segment of the eye) the mirror terms heavily

OCIS codes: (170.4500) Optical coherence tomography; (170.3880) Medical and biological imaging; (170.4580) Optical diagnostics for medicine

Europe PMC Funders Author Manuscripts

decrease the image quality and make it difficult to interpret the collected data. Furthermore, the sensitivity decrease of SD-OCT with distance from the zero position [3,7] makes a differentiation between positive and negative distances highly desirable because this would allow to place the object within the most sensible measurement range near the reference mirror position.

A solution to this problem is to measure the phase of the spectral interferometric signal, thus providing access to the complex scattered field [8]. An inverse Fourier transform of the complex data directly provides the true object structure, eliminating any mirror terms. Various approaches to achieve full range complex (FRC) SD-OCT were reported, essentially employing different variants of phase shifting interferometry [8-13]. These methods require the recording of 2-5 A-scans at a given transversal sampling location, whereby the reference phase is shifted between the individual A-scans by piezo-driven reference mirrors or acousto-/electro-optic phase modulators. The disadvantages of these methods are that additional components (piezo drive, acousto-/electro-optic modulators) are required and measurement speed is reduced by the requirement of multiple A-scans.

Another scheme of FRC SD-OCT uses a linearly increasing phase shift generated by uniform movement of a piezo-driven reference mirror during a B-scan [14,15]. Complex data are obtained by a combination of Fourier transforms or a Hilbert transform in transverse direction. This method (which could also be realized using acousto-/electro-optic phase modulators) has the advantage of requiring only one A-scan per measurement location, thus improving imaging speed. However, an additional phase shifting element (piezo drive) that also requires correct triggering is still required, adding to system costs and complexity.

In this paper, we demonstrate a new method of FRC SD-OCT that is based on the technique reported in refs. [14,15], however, avoids any additional phase shifting element. Instead, the phase shifting is introduced by the galvo scanner that is used for x-scanning the sampling beam, a technique initially developed to generate a carrier frequency for en face OCT [16]. A slight deviation of the sampling beam from the pivot axis of the x-scanner causes a path length modulation during x-scanning [17], introducing the required phase shift. In the following sections, we present the method, quantify the mirror image suppression as a function of system parameters, and demonstrate the performance of the system in a human anterior chamber in vivo.

2. Methods

2.1 Complex SD-OCT signal reconstruction

In SD-OCT, depth profiles of back-scattered intensity, $I(z)$, are retrieved by an inverse Fourier transform of the spectral interferogram, $\hat{S}(k)$. Since only the real part of the complex-valued spectrum, $S(k) = \mathrm{Re}[\hat{S}(k)]$, is recorded with the spectrometer, its inverse Fourier transform $\mathrm{FT}^{-1}\{S(k)\}$ is Hermitian which results in an image symmetric about zero phase difference.

In FRC SD-OCT, retrieval of the complex-valued spectral data and thus reconstruction of OCT images free of artifacts caused by unresolved sign of path length differences with respect to the reference mirror, is enabled by obtaining the phase of the spectral interferograms. The FRC SD-OCT algorithm we use is based on the techniques reported in refs. [14] and [15].

The spectral data corresponding to an OCT B-scan image (as shown in Fig. 1(a), step (i)) are built up by a 2D array $S(x,k)$ of data points in the plane spanned by wave number k and transversal scanning position x. Each column represents the (real-valued) spectral

interferogram of one A-scan, whereas each line contains the spectral data recorded at one spectrometer pixel, i.e. for one wave number k, as the probe beam is scanned transversally (in x-direction) over the sample. (Inverse) Fourier transforms of the spectral data can now be applied in either k-direction (column by column; blue section in Fig. 1(a)) or x-direction (line by line; red section in Fig. 1(a)). An inverse Fourier transform of one column results in the A-scan signal (spatial domain signal in z-direction) for one lateral measurement position x, $\mathrm{FT}_{k\to z}^{-1}\{S(x = constant,k)\} = I(x = constant,z)$, whereas a Fourier transform of one line yields a spectrum in spatial frequency domain, $\mathrm{FT}_{x\to u}\{S(x,k = constant)\} = B(u,k = constant)$, with u being the Fourier conjugate of x.

In OCT B-scan images recorded from motionless samples, the Doppler phase shift Φ between adjacent A-scans will be zero. By Fourier transforming such a B-scan's spectral data line by line, one will obtain a spectrum $B(u,k)$ centered at the origin $u = 0$ in spatial frequency domain as illustrated in the bottom right corner of Fig. 1(a). The shape and width of $B(u,k)$ is dependent on the transversal geometry of the sample object.

However, if the phase is shifted by a constant amount of Φ from A-scan to A-scan resulting in a linearly increasing phase as the probe beam is transversally scanned, the outcome of the Fourier transform in transverse direction x will be different (cf. Fig. 1(b), step (i)): Due to the Fourier shift theorem, the contributions of the OCT signal in spatial frequency domain, $B(u,k)$, which originate from object structure, will be shifted away from zero frequency to both the negative and positive frequency range owing to phase shifts of −Φ and +Φ respectively:

$$FT_{x\to u}\left\{Re\left[\widehat{S}(x,k)\exp\left(i\left[\delta\phi/\delta x\right]x\right)\right]\right\} = \bar{B}(u-\delta\phi/\delta x,k) + B(u+\delta\phi/\delta x,k) \quad (1)$$

where $\delta\Phi$ is the phase shift when the beam is scanned over a distance δx. Like after performing a Fourier transform along k, also the result of the Fourier transform along x in equation (1) will be Hermitian, i.e. symmetrical about the zero frequency position, since the Fourier transform of the real-valued spectral interferogram is performed. Both spectra $B(u,k)$ and $\bar{B}(u,k)$ contain the same information on the OCT signal in spatial frequency domain, but – in contrast to a Fourier transform along k – the two contributions can be separated by means of an appropriately sized phase shift Φ in order to allow for reconstruction of the complex-valued spectral interferogram.

Since both terms on the right-hand side of equation (1) contain the same complex-valued information in spatial frequency domain, the complex-valued spectrum $\widehat{S}(u,k)$ can now be reconstructed by performing the inverse Fourier transform back to the original domain for just one of the two terms. For this purpose, the Heaviside step function $\Theta(u)$ is applied, such that only the rightmost term of equation (1) remains (step (ii) in Fig. 1(b)). Now, for reasons of energy conservation, the data have to be scaled by a factor of 2. A subsequent inverse Fourier transform line by line back to the original domain finally yields the complex-valued spectral interferograms, $\hat{S}(x,k)$ from which the full range OCT image $I(x,z)$ can bex calculated by inversely Fourier transforming the data column by column. In Fig. 1(b), this is indicated by steps (iii) and (iv).

The total reconstruction of the complex-valued spectral interferogram is possible provided that the following two conditions hold: First, the total width of the spectrum $B(u)$ must not exceed half of the Fourier space. Second, in order to achieve a clear separation of the shifted spectra $B(u)$ and $\bar{B}(u,k)$ in spatial frequency domain, the size of the phase shift Φ is preferably chosen such that the spatial frequency band covered by $B(u)$ will be positioned near the center of the negative and positive half-spaces of u which is the case when phase

shifts $\Phi = \pi/2$ are applied between consecutive A-scans. In case one or both of the conditions do not hold, the spectrum $B(u)$ shifted to the positive spatial frequency range will overlap into the negative spatial frequency range. Similarly, the spectrum $\bar{B}(u,k)$ shifted to the negative spatial frequency range will overlap into the positive range. After the Heaviside function is applied in spatial frequency domain, this overlapping portion will contribute to a complex-valued signal at $-z$ if the actual structure is at $+z$ and vice versa. Dependent on the fraction of $B(u)$ extending to the other half space, the suppression of the mirror term will be more or less efficient.

The same result is achieved when the Hilbert transform is used for reconstruction of the analytic signal [15], which is graphically pointed out by the green arrow in Fig. 1(b). Resuming the calculation steps above, the complex-valued signal for each wave number k is given by

$$\widehat{S}(x) = 2FT_{u\to x}^{-1}\{\Theta(u)\,FT_{x\to u}[S(x)]\}. \quad (2)$$

For the Heaviside function, the identity $\Theta(u) = \mathrm{FT}_{x\to u}\{\tfrac{1}{2}\delta(x) + i/(2\pi x)\}$ can be used, where $\delta(x)$ denotes the Dirac delta function [18]. With the definition of the Hilbert transform $\mathrm{HT}\{S(x)\} = (-\pi x)^{-1} * S(x)$, where * denotes the convolution, the complex-valued spectral interferogram can be expressed as [18]

$$\widehat{S}(x) = S(x) - iHT\{S(x)\}. \quad (3)$$

In ref. [15] it was shown, that $\hat{S}(x)$ can be obtained as the analytic representation of $S(x)$ with the quadrature components yielded by the Hilbert transform provided that the highest spatial frequency component of $B(u)$ is less than the modulation frequency, i.e. $\delta\Phi/\delta x$. This condition, which was referred to as Bedrosian's theorem in [15], is equal to the restriction made above for the total complex signal reconstruction.

It should be mentioned that – as the first step of data processing – any DC component of the spectral data has to be removed prior to the Hilbert transform since the Hilbert transform may only be applied to AC data.

2.2 Generation of modulation frequency

In order to generate phase shifts, usually devices such as acousto-/electro-optic modulators or piezo-driven reference mirrors have been used in FRC SD-OCT [8-15]. The FRC SD-OCT method presented here omits any additional phase modulating devices by adapting a technique originally developed by Podoleanu et al. [17] for generating a stable carrier frequency for en face scanning OCT. The sample beam geometry is adjusted in such a manner that the light beam coming from the interferometer beam splitter hits the galvo scanner mirror used for x-scanning slightly aside its pivot axis (Fig. 2). During the x-scan, the sample beam path length is changed depending on the mechanical scan angle $\Delta\alpha$. Under the assumption of small scanning angles and using Taylor series expansions, the path length imbalance Δz can be approximated as [17]

$$\Delta z \approx s\Delta\beta \quad (4)$$

where as s the offest of the mirro' axis of roatation with to the beam (henceforth called mirror offset s) and $\Delta\beta$ is the optical tilt angle ($\Delta\beta = 2\Delta\alpha$). The resulting phase shift between two adjacent A-scans can be calculated using $\Phi = 4\pi\Delta z/\lambda$ as

$$\Phi = \frac{4\pi \cdot s \cdot \Delta\beta_{\max}}{N \cdot \lambda} \quad (5)$$

with N being the number of A-scans per B-scan, λ the central wavelength of the light source and $\Delta\beta_{\max}$ being the total scanning angle. For given transversal scan range and pixel number, the galvo mirror offset s necessary to obtain a phase shift of e.g. $\Phi = \pi/2$ can now be derived from equation (5).

2.3 Experimental setting

A sketch of our FRC SD-OCT setup is shown in Fig. 3. A superluminescent diode (Superlum, Russia) centered at 840 nm with a *FWHM* bandwidth of 50 nm was used as a light source. In the sample arm of the free-space Michelson interferometer, an *x*-*y* galvanometer scanner pair (Galvoline, Italy) was employed for scanning the beam, which was focused by an achromatic lens with focal length of 80 mm, across the sample. The scanner unit was mounted on an *x*-*y* translation stage driven by micrometer screws to provide exact adjustment of the mirror offset and thus of the phase shift. A variable neutral density filter was used in the reference arm in order to operate the spectrometer CCD camera close to the saturation limit. After recombination of the sample and reference beams, the interfering beam was coupled into a single mode fiber and guided to the spectrometer unit, where it was collimated and directed onto a transmission grating (Wasatch, USA) with 1200 lines/mm. The dispersed spectrum was focused by an achromatic lens of 200 mm focal length and recorded with a 2048 element CCD camera (Atmel, France) with 14 × 14 μm^2 pixel size. The spectrometer settings provided a spectral resolution of 0.051 nm and a total depth range of 6.6 mm (2 × 3.3 mm). The spectral data were transferred to computer memory via CameraLink and a high speed frame grabber board (National Instruments, USA).

With a probing power of 1.3 mW and an integration time of 100 μs, a sensitivity of 101 dB was measured close to the zero delay. During the sensitivity measurement, the galvo scanner was in a fixed position. Due to the finite spectral resolution of the spectrometer sensitivity dropped by 13 dB at $z = \pm 2.5$ mm.

Several steps of post-processing were performed. After fixed pattern noise removal (including DC removal), the 2D spectral data were line-by-line Hilbert transformed along *x* in order to calculate the quadrature components as described in section 2.1. Once the complex spectral data had been reconstructed, they were rescaled from linear sampling in λ-space to equal sampling intervals in *k*-space. A final inverse Fourier transform of every A-line's complex spectral interferogram resulted in the OCT B-scan image which was displayed on a logarithmic grey scale.

3. Results

In order to test the performance of the galvo scanner induced phase shifting technique different measurements were performed. For these measurements the weakly scattering surface of a black-anodized aluminum part was used as a sample. With a power of 1.3 mW onto the sample and a camera integration time of 100 μs, B-scan images consisting of 1000 A-lines were recorded. For a scan angle of 12° the image width was 15 mm. The dynamic range of the images was measured to be 45 dB. By use of the translation stage of the galvo scanner assembly the mirror offset s was set to 24 equidistant positions ranging from $s = -1.03$ mm to $s = 1.12$ mm around the *x*-scanner's pivot axis. For each step, B-scan images were recorded and hereupon, the phase shift at the surface of the sample object caused by the respective mirror displacement was calculated. The results of these measurements are

Europe PMC Funders Author Manuscripts

plotted in Fig. 4 for three different positions of the sample surface with respect to the reference mirror. A linear relationship of mirror offset and induced phase shift between adjacent A-scans can be observed.

The linearity of the induced path length modulation is demonstrated in Fig. 5. For a mirror offset of 0.56 mm, the cumulated phase shift along one transversal line is plotted versus A-scan number. A linear fit with a slope of 1.633 rad/A-line (which slightly deviates from the desired value $\Phi = \pi/2 = 1.571$ rad) is shown in red. The offset of −41.553 rad between the measured, unwrapped curve and the fitted curve arises from the back snapping of the galvo scanner. When the scanner is driven by a short negative ramp during the back snapping, complete interference fringe washout – equivalent to total signal loss – occurs. Therefore, for the first ~30 A-scans in Fig. 5, also no phase shift is registered and the offset of 41.553 rad ($\sim 30 \cdot \pi/2$) arises.

The efficiency of complex conjugate suppression as a function of the induced phase shift was investigated using the same data. In Fig. 6, the extinction ratio (*ER*), i.e. the ratio of the surface signal and its complex conjugate on the other side of the zero path delay, is plotted against mirror offset *s*. Extinction ratios better than −30 dB can be observed for phase shifts of $-\pi/2$ and $+\pi/2$, respectively. When going from negative to positive mirror offsets, the resulting phase shifts cause the extinction ratio to flip, i.e. with respect to *z* the reconstructed full range image will be oriented the opposite way around. The effect can be understood taking into account $\exp[i\pi] = -1$. No suppression of the complex conjugate artifact – an extinction ratio of 0 dB – is to be observed for values of $\Phi = M\pi$ with *M* being an integer.

Considering the theoretical description of the complex signal reconstruction shown in section 2, for $B(u,k) = B(k)^* \delta(u)$ (i.e., assuming a transversally homogeneous object geometry), any phase shift $\Phi \neq M\pi$ should ideally lead to total suppression of complex conjugate signals. Choosing phase shifts in the interval of $(M\pi\ (M+1)\pi)$, reconstructed image features will flip from $+z$ to $-z$ and vice versa for even and odd values of *M*, respectively.

Different physical effects reduce the theoretical performance of our phase shifting technique. First, resulting from the wavelength dependency of equation (5), a chromatic phase error [13] will arise when broadband light is being used. The transversal lines of the 2D spectral interferogram will be subject to different phase shifts in the order of $\Delta\Phi(\lambda) = \Phi\Delta\lambda/\lambda$. For the light source used in our experiment, the range of phase shifts is $\Delta\Phi(\lambda) \sim \Phi \cdot 0.06$ When s is set such that $\Phi = \pi/2$, the phase shifts will cover a rather narrow range of ~5° FWHM. However, for larger phase shifts Φ also the chromatic broadening of the covered range of phase shifts is increasing.

A second effect, by which the range of phase shifts applied is broadened, originates from the non-zero diameter of the collimated beam at the galvo mirror surface. When the sample beam hits the galvo scanner mirror, a Gaussian distribution of phase shifts Φ is produced due to the Gaussian intensity distribution in the beam's cross-section incident at different offsets *s* from the pivot axis. For a mirror offset *s* with respect to the beam center, which produces a central phase shift Φ_0, the arising distribution of phase shifts *G* can be approximated as

$$G(\Phi, \Phi_0(s), \Delta\Phi_{FWHM}) = \sqrt{\frac{4\ln 2}{\pi \cdot \Delta\Phi_{FWHM}^2}} \exp\left[-\frac{4\ln 2(\Phi - \Phi_0(s))^2}{\Delta\Phi_{FWHM}^2}\right] \quad (6)$$

where $\Phi_0(s) = 2k \cdot s \cdot \Delta\beta_{\max} / N$ is the central phase shift as defined in section 2.2 and $\Delta\Phi_{FWHM} = 2k \cdot BD \cdot \Delta\beta_{\max} / N$ is the full width at half maximum (*FWHM*) of the

distribution caused by a *FWHM* beam diameter *BD*. Now, taking into account that any phase shift $\Phi \in (M\pi, (M+1)\pi)$ will reproduce the image at either depth $+z$ or $-z$ dependent on the parity of *M*, all components shifted by Φ in an interval with odd *M* will give rise to a signal on one side of zero path delay $z = 0$, whereas all phase shifts in an even-*M*'ed interval will contribute to a signal on the other side. Since the extinction ratio *ER* was defined as the quotient of the signal fraction on one side of zero path delay and the signal fraction on the other side, one can theoretically estimate *ER* by integrating positively and negatively shifted fragments of *G* and calculating their ratio as

$$ER = \left(\frac{\int_{-\infty}^{\infty} \Theta(\sin\Phi)\,[G(\Phi, \Phi_0(s)) + NC(\Phi)]\,d\Phi}{\int_{-\infty}^{\infty} \Theta(\sin(-\Phi))\,[G(\Phi, \Phi_0(s)) + NC(\Phi)]\,d\Phi} \right)^2 \quad (7)$$

The first element of the integrands, Θ(sin(±Φ)), is the Heaviside function applied to the sine of Φ and −Φ; *NC*(Φ) denotes the noise contribution of the phase shifts. The numerator contains all contributions of *G* for even values of *M*; the denominator in turn contains the contributions for odd-valued *M*.

The theoretical model for mirror term suppression was employed for an estimation of *ER*. For this first approximation of *ER*, the influence of the chromatic phase error mentioned above was ignored because it is considerably smaller. By means of a beam profiler (Dataray, USA), the beam's *FWHM* diameter *BD* was measured to be ~500 μm. Using this value for *BD* and the set parameter values used for the *ER* measurements, a theoretical curve *ER* (dashed plot in Fig. 6) was computed with equations (6) and (7). NC(Φ) = 0 was assumed. It can be seen in Fig. 6 that the measured values are in good agreement with the theoretical prediction; still, slight deviations are observable. The minimum and the maximum of the theoretical curve are closer to $s = 0$ than the results of the measurement, which indicates that the measured central phase shifts Φ_0 are smaller than the expected ones. An actually slightly smaller total scanning angle $\Delta\beta_{max}$ which is proportional to Φ_0 might be responsible for this deviation.

As a third effect, the width of the distribution of spatial frequencies due to the transverse object structure has to be considered. For a sample without any variations of structure along the B-lines along *x*-direction (to which our test object can be approximated), the spectrum in spatial frequency domain can be expressed by $B(u,k) = B(k)^* \delta(u)$ with $\delta(u)$ being the Dirac delta function. Of course, for sample structures exhibiting variations along *x*-direction (as it is usually the case for biological tissue), the spectrum $B(u,k)$ will cover the corresponding range in *u*-domain. It was mentioned as one condition for total complex signal reconstruction in section 2.1 that the range covered by $B(u,k)$ must not exceed half of the spatial frequency space. Any overlap of the spectral components in the positive and negative ranges will induce complex conjugate artifacts. Hence, for structures with a broad spectrum in spatial frequency domain an inferior *ER* is to be expected.

Since the method discussed in this paper is a dynamic phase shifting technique (i.e., the phase is shifted not stepwise but continuously), one has to consider fringe washout as a source of signal degradation. The larger mirror offset *s* is chosen, the higher will be the speed of the scanning mirror and the stronger will be the fringe washout. Yun et al. have first described this movement-induced fringe washout as a *SNR* degrading factor of $\sin^2(\Phi_0/2)/(\Phi_0/2)^2$ with Φ_0 being the phase shift induced by axial movement [19]. For phase shifts of $|\Phi_0| \leq \pi/2$, as they are used in this paper, the *SNR* penalty caused by fringe washout will be less than 1 dB; for $|\Phi_0| = \pi$, the theoretical signal loss amounts to almost 4 dB. When even larger phase shifts are produced, signal degradation will considerably reduce image quality. Also, it is crucial for the algorithm to have a certain phase relation between

neighboring A-scans; therefore, the distance between adjacent A-scans must not exceed the focal beam diameter.

In order to evaluate the FRC SD-OCT system performance for in vivo imaging, we imaged the anterior chamber of the eye of a healthy human volunteer. The integration time of the spectrometer CCD camera was set to 100 μs per A-scan; the sample was exposed to a light power of 1.3 mW which is well below the safety limits given by the ANSI and IEC standards for the safe use of lasers [20,21]. For the total scanning angle of 12° the mirror offset s was adjusted such that a phase shift of $\pi/2$ required for efficient removal of the complex conjugate artifact was generated. The images shown in Fig. 7 show results derived from the same spectral data. For Fig. 7(A), the spectral interferograms were (after fixed pattern noise removal and remapping to k-space) processed by an inverse FFT of each real-valued spectral interferogram (conventional SD-OCT). The true object structure is obscured by the overlapping mirror image. Figure 7(B) was calculated from the same data; however, here the additional processing step described in section 2.1 was performed in order to recover the complex valued spectral data. Two remaining transverse line artifacts due to an internal reflection and the complex signals' DC terms that could not be removed by the algorithm were eliminated by cutting out the respective B-lines and interpolating the intermediate values [22]. As can be seen in Fig. 7(B), the complex conjugate mirror image could sufficiently be suppressed.

4. Discussion

4.1 Comparison with two-frame algorithm

The high speed FRC SD-OCT system presented in this paper relies on the generation of phase shifts induced by the galvo mirror scanning in x-direction. The such generated phase difference between adjacent A-scans gives the best results, i.e. the strongest suppression of the complex conjugate artifact, for values of $\pi/2$ or $-\pi/2$. This is visible in the measured data of Fig. 6; and also in the theoretical description of the method these values were pointed out to be the favorable choice.

Recently, a fast FRC SD-OCT technique employing an electro-optic phase modulator (EOM) for generating phase shifts of $\pi/2$ has been reported [12]. By use of such modulation, the complex valued data was calculated and the full-range OCT signals could be reconstructed. We applied the reconstruction algorithm presented in that paper to the galvo mirror modulated spectral data of an OCT B-scan image in order to compare the two algorithms. In Fig. 8(A) the OCT image obtained by an inverse FFT of the real-valued spectral data is shown. The data of B-scan images shown in Figs. 8(B) and 8(C) have been processed using the two-frame algorithm of ref. [12] and the complex reconstruction technique discussed in this paper, respectively. The computation time on a Pentium 4 CPU operating at 3.2 GHz for calculating the 1000 complex lines of the image (including also noise removal and remapping) is ~3 seconds for both algorithms implemented in LabView. In both images, the artifacts could be removed, however, especially in regions where the images overlap in Fig. 8(A), shadow-like remainders of the mirror images are still visible after the two-frame algorithm had been applied (Fig. 8(B)), which are not apparent in Fig. 8(C).

4.2 Influence of sample motion

The FRC SD-OCT algorithm used is based on constant phase shifts of Φ from one transversal pixel to the next. Any sample movement in axial direction will result in an additional phase shift $\Phi_s = 4\pi\, v_x \Delta t/\lambda$, where v_x is the velocity of the axial sample movement and Δt is the time between two A-scans. The total phase shift will be $\Phi_{eff} = \Phi_s +$

Φ. With increasing axial sample motion, the mirror image will be less suppressed. For an additional shift of $\Phi_S = \pi/2$, the mirror terms have the same intensity as the original signal. If the additional phase shift amounts to $\Phi_S = \pi$, any sample structure at depth $+z$ will be flipped to $-z$. With $v(\Phi_s=\pi) = \lambda/(4\Delta t)$ the axial sample velocity necessary for such an image flip can be estimated as ~2 mm/s for the image parameters we used for imaging the anterior chamber (λ = 840 nm; Δt = 100 μs). It is clear that further reduction of the time Δt elapsing between neighboring A-scans would proportionally improve the method's robustness against sample movements. Figure 9 shows an OCT B-scan image that was distorted by sample (subject) movement. In the left part of the image motion artifacts manifesting in image flips are clearly visible.

5. Conclusion

We have presented FRC SD-OCT free of additional phase shifting devices. The phase modulation necessary for complex signal reconstruction is induced during scanning the probe beam over the sample in *x*-direction. A slight displacement of the sample beam with respect to the galvanometer mirror's axis of rotation gives rise to a path length modulation and hence to a shift of the interferometric signal's phase. From such modulated data, recovery of the complex spectral data and finally increasing the accessible imaging depth by a factor of 2 was enabled by an algorithm based on the Hilbert transform.

The feasibility of the technique for high speed imaging of biological tissue was discussed and demonstrated in human anterior eye segments in vivo. The results validate the FRC SD-OCT method as a promising technique that can easily be implemented in any existing SD-OCT system to double the imaging range without any additional expenses.

Acknowledgments

The authors wish to thank H. Sattmann and C. Wölfl for technical assistance. Financial support of the Austrian Science Fund (FWF grants P16776-N02 and L126-N08) is gratefully acknowledged.

References and links

1. Huang D, Swanson EA, Lin CP, Schuman JS, Stinson WG, Chang W, Hee M, Flotte T, Gregory K, Puliafito CA, Fujimoto JG. Optical coherence tomography. Science. 1991; 254:1178–1181. [PubMed: 1957169]
2. Fercher AF, Drexler W, Hitzenberger CK, Lasser T. Optical coherence tomography-principles and applications. Rep. Prog. Phys. 2003; 66:239–303.
3. Leitgeb RA, Hitzenberger CK, Fercher AF. Performance of Fourier Domain vs. Time Domain optical coherence tomography. Opt. Express. 2003; 11:889–894. http://www.opticsexpress.org/abstract.cfm?URI=OPEX-11-8-889. [PubMed: 19461802]
4. de Boer JF, Cense B, Park BH, Pierce MC, Tearney GJ, Bouma BE. Improved signal to noise ratio in spectral domain compared with time domain optical coherence tomography. Opt. Lett. 2003; 28:2067–2069. [PubMed: 14587817]
5. Choma MA, Sarunic MV, Yang C, Izatt JA. Sensitivity advantage of swept source and Fourier domain optical coherence tomography. Opt. Express. 2003; 11:2183–2189. http://www.opticsexpress.org/abstract.cfm?URI=OPEX-11-18-2183. [PubMed: 19466106]
6. Fercher AF, Hitzenberger CK, Kamp G, El- Zaiat SY. Measurement of intraocular distances by backscattering spectral interferometry. Opt. Commun. 1995; 117:43–48.
7. Häusler G, Lindner MW. Coherence radar and spectral radar - new tools for dermatological diagnosis. J. Biomed. Opt. 1998; 3:21–31. [PubMed: 23015002]
8. Fercher AF, Leitgeb R, Hitzenberger CK, Sattmann H, Wojtkowski M. Complex spectral interferometry OCT. Proc. SPIE. 1999; 3564:173–178.

9. Wojtkowski M, Kowalczyk A, Leitgeb R, Fercher AF. Full range complex spectral optical coherence tomography technique in eye imaging. Opt. Lett. 2002; 27:1415–1417. [PubMed: 18026464]
10. Targowski P, Wojtkowski M, Kowalczyk A, Bajraszewski T, Szkulmowski M, Gorczynska I. Complex spectral OCT in human eye imaging in vivo. Opt. Commun. 2004; 229:79–84.
11. Leitgeb RA, Hitzenberger CK, Fercher AF, Bajraszewski T. Phase shifting algorithm to achieve high speed long depth range probing by frequency domain optical coherence tomography. Opt. Lett. 2003; 28:2201–2003. [PubMed: 14649941]
12. Götzinger E, Pircher M, Leitgeb RA, Hitzenberger CK. High speed full range complex spectral domain optical coherence tomography. Opt. Express. 2005; 13:583–594. http://www.opticsexpress.org/abstract.cfm?URI=OPEX-13-2-583. [PubMed: 19488388]
13. Bachmann A, Leitgeb R, Lasser T. Heterodyne Fourier domain optical coherence tomography for full range probing with high axial resolution. Opt. Express. 2006; 14:1487–1496. http://www.opticsinfobase.org/abstract.cfm?URI=oe-14-4-1487. [PubMed: 19503473]
14. Yasuno Y, Makita S, Endo T, Aoki G, Itoh M, Yatagai T. Simultaneous *B*–*M*-mode scanning method for real-time full-range Fourier domain optical coherence tomography. Appl. Opt. 2006; 45:1861–1865. [PubMed: 16572705]
15. Wang RK. In vivo full range complex Fourier domain optical coherence tomography. Appl. Phys. Lett. 2007; 90:054103.
16. Podoleanu AG, Dobre GM, Webb DJ, Jackson DA. Coherence imaging by use of a Newton rings sampling function. Opt. Lett. 1996; 21:1789–1791. [PubMed: 19881802]
17. Podoleanu AG, Dobre GM, Jackson DA. En-face coherence imaging using galvanometer scanner modulation. Opt. Lett. 1998; 23:147–149. [PubMed: 18084441]
18. Bracewell, RN. The Fourier transform and its applications. 3rd ed.. McGraw-Hill; New York: 2000.
19. Yun SH, Tearney G, de Boer J, Bouma B. Motion artifacts in optical coherence tomography with frequency-domain ranging. Opt. Express. 2004; 12:2977–2998. http://www.opticsinfobase.org/abstract.cfm?URI=oe-12-13-2977. [PubMed: 19483816]
20. American national standard for safe use of lasers. Laser Institute of America; Orlando: 2000. ANSI Z 136.1
21. InternationaI Electrotechnical Comission. Safety of laser products - Part 1: Equipment classification and requirements. IEC; 2001. IEC 60825-1 Ed. 2
22. Bachmann AH, Michaely R, Lasser T, Leitgeb RA. Dual beam heterodyne Fourier domain optical coherence tomography. Opt. Express. 2007; 15:9254–9266. http://www.opticsinfobase.org/abstract.cfm?URI=oe-15-15-9254. [PubMed: 19547267]

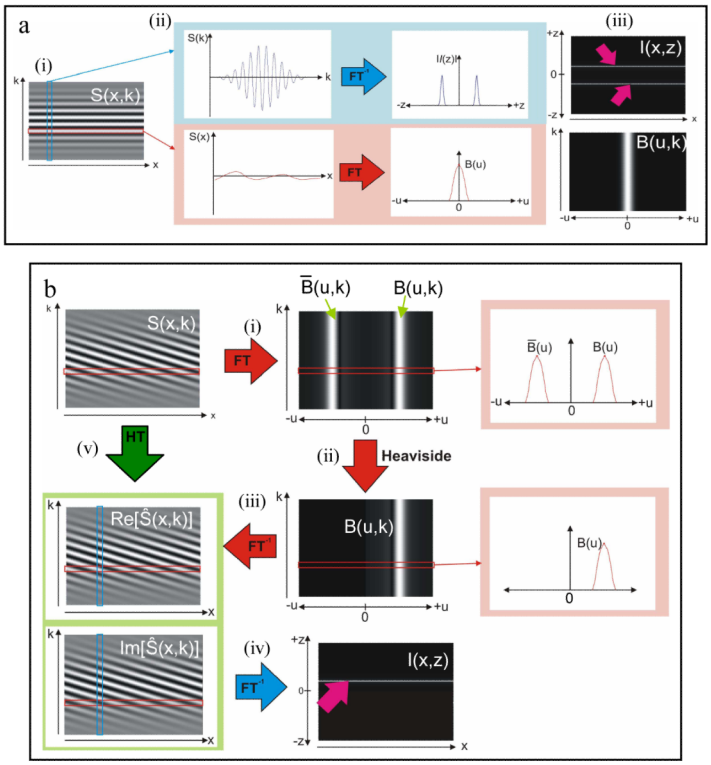

Fig. 1.

Illustration of conventional SD-OCT and the FRC-SD-OCT method. (a) SD-OCT: (i) Real-valued 2D spectral interferogram *S(x,k)*; (ii) inverse Fourier transform (FT^{-1}) of a column (top, blue) and FT of a line of *S(x,k)* (bottom, red); (iii) B-scan image *I(x,z)* suffering from mirror term (top) and spectrum in spatial frequency domain *B(u,k)* (bottom). (b) FRC-SD-OCT: (i) A FT line-by-line of the phase-shifted real-valued 2D spectral interferogram yields the spectra *B(u)* shifted away from $u = 0$; (ii) subsequent application of the Heaviside function; (iii) now, an inverse FT results in the complex-valued spectral interferogram $\hat{S}(x,k)$ (green box), from which the unambiguous full-range image *I(x,z)* can be calculated by column-wise FT^{-1} (iv). (v) Steps (i)-(iii) can be replaced by a Hilbert transform (HT).

Europe PMC Funders Author Manuscripts

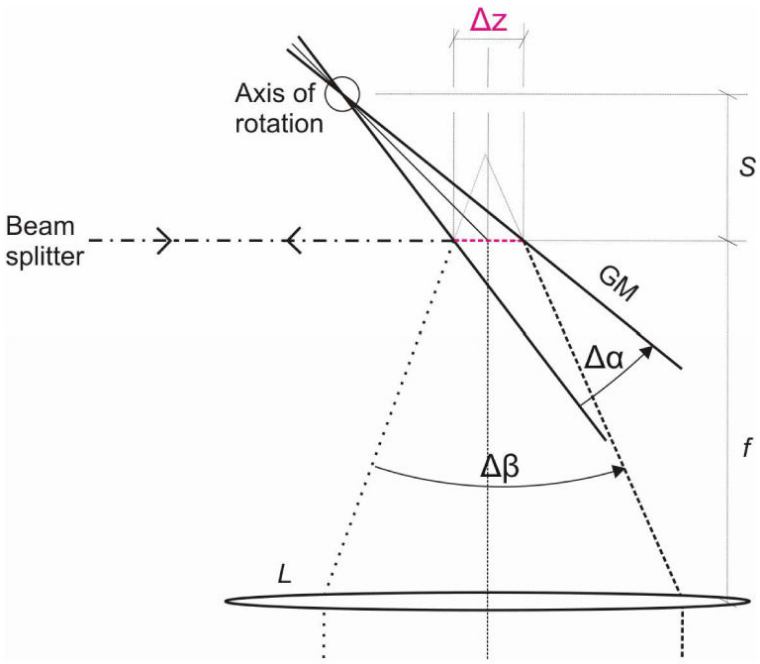

Fig. 2.

Sketch of the sample beam geometry. For a tilt of the galvo scanner mirror (GM) by an angle $\Delta\alpha$, the sample beam is deflected by $\Delta\beta$ from its original direction. If the mirror's axis of rotation is shifted by the mirror offset s orthogonal to the incoming ray, the sample beam path will be altered by Δz. f denotes the focal length of the imaging lens (L).

Europe PMC Funders Author Manuscripts

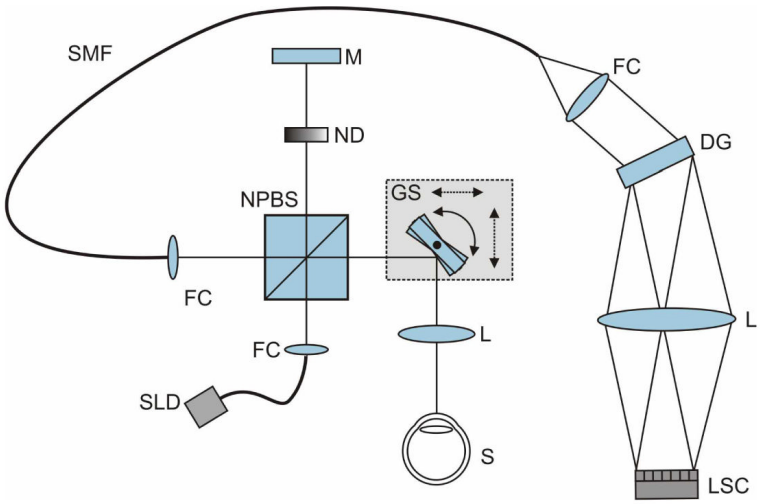

Fig. 3.

Sketch of FRC SD-OCT system. Interferometer: SLD, super luminescent diode; FC, fiber coupler; NPBS, non polarizing beam splitter; ND, variable neutral density filter; M, reference mirror; GS, galvo scanner unit mounted on *x*-*y* translation stage; L, lens; S, sample. SMF, single mode fiber. Spectrometer: DG, diffraction grating; LSC, line scan CCD camera.

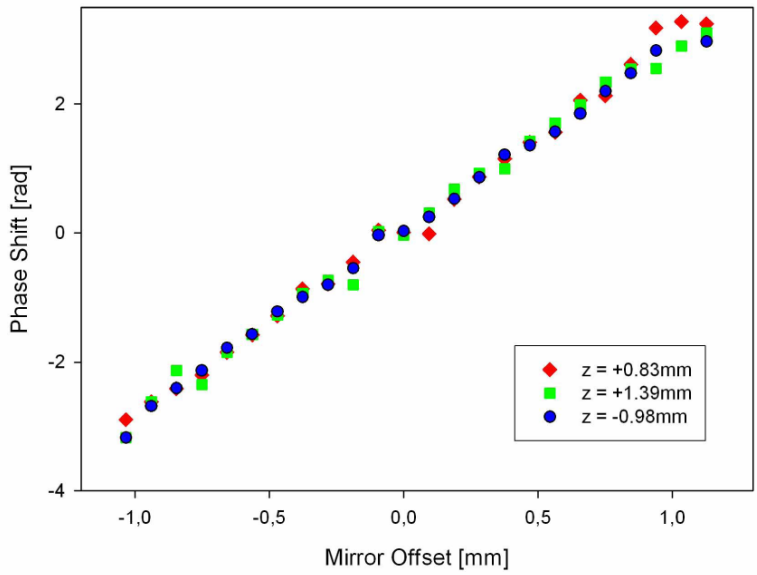

Fig. 4.

Measured phase shift Φ as a function of mirror offset *s* for three different depth positions *z*. A linear relationship between *s* and Φ can be observed.

Europe PMC Funders Author Manuscripts

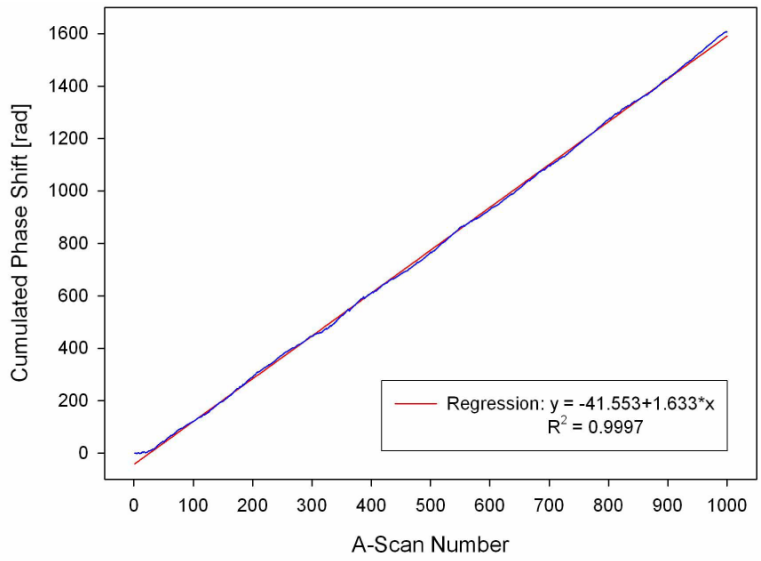

Fig. 5.

Cumulated (unwrapped) phase shift along a transverse line of a B-scan. The red line is a linear fit with a slope of 1.633 rad/A-scan. R^2 = 0.9997 is the coefficient of determination.

Europe PMC Funders Author Manuscripts

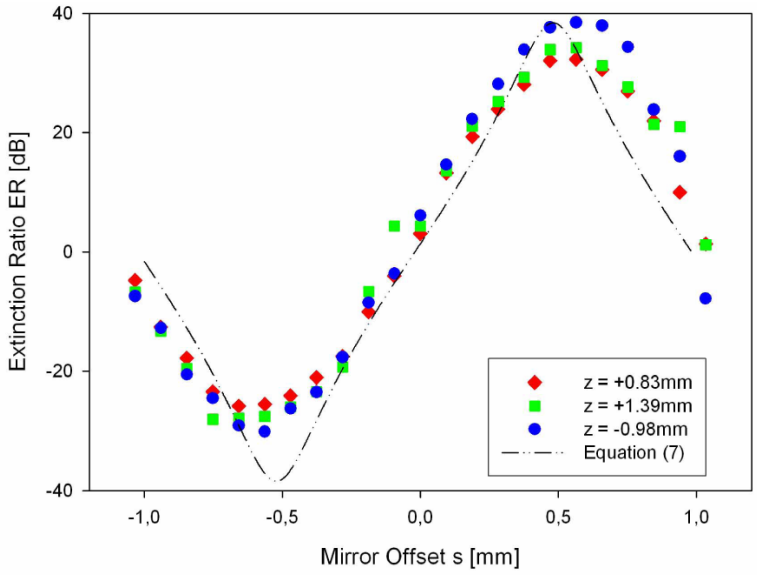

Fig. 6.

Extinction ratio of complex conjugate artifact as a function of mirror offset *s* measured for three different depth positions. For mirror displacements corresponding to phase shifts of $-\pi$, 0, and π, the mirror signal is not suppressed, i.e. the extinction ratio is 0 dB. At a mirror offset of $s = -0.56$ mm ($\Phi = -\pi/2$) extinctions better than −30 dB were achieved. When the mirror was displaced by the same distance on the other side of the zero position, $s = +0.56$ mm ($\Phi = +\pi/2$), the extinction amounted to the reciprocal value. The dashed black curve was computed using equation (7) and shows theoretically expected extinction ratios *ER*.

Europe PMC Funders Author Manuscripts

Europe PMC Funders Author Manuscripts

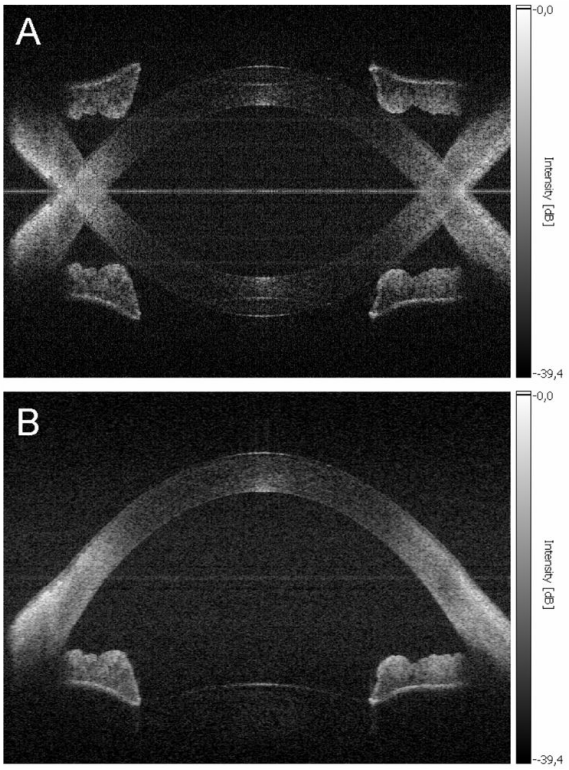

Fig. 7.

B-scan images of human anterior eye segment in vivo. (A) Tomogram obtained by inverse FFT of the real-valued spectral data. (B) Full-range image obtained by reconstruction of the complex-valued spectral data. Image size: 14 (x) × 6.6 (z, optical distance) mm^2. The displayed dynamic range is 39.4 dB for both images.

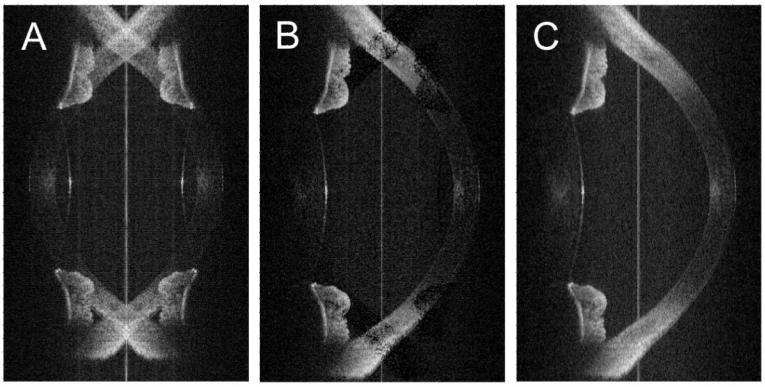

Fig. 8.

Tomograms of human anterior chamber in vivo. (A) Image obtained by inverse FFT of the real-valued spectral data. (B) Tomogram obtained by application of the 2-frame algorithm presented in ref. [12]. Shadow-like artifacts remain in overlapping regions. (C) Image obtained using the Hilbert-transform based algorithm. Note that here the line artifact at zero path delay was not removed. All images have been derived from the same raw data. Image size: 14 (x) × 6.6 (z, optical distance) mm^2.

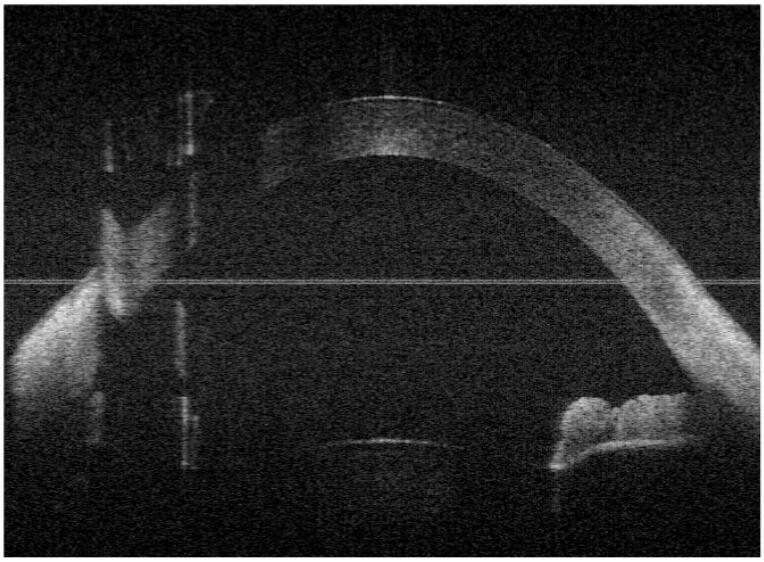

Fig. 9.
B-scan image of human anterior chamber in vivo illustrating the influence of involuntary movement of the subject's eye. In the left part of the image the additional phase shift due to axial motion gives rise to flips of the image. Size of image: 14 (x) × 6.6 (z, optical distance) mm^2.

Europe PMC Funders Author Manuscripts